

# Thermal Cycling and High-Temperature Corrosion Tests of Rare Earth Silicate Environmental Barrier Coatings

Émilien Darthout<sup>1</sup> · François Gitzhofer<sup>1</sup>

Submitted: 25 October 2016 / in revised form: 31 July 2017 / Published online: 12 September 2017  
© ASM International 2017

**Abstract** Lutetium and yttrium silicates, enriched with an additional secondary zirconia phase, environmental barrier coatings were synthesized by the solution precursor plasma spraying process on silicon carbide substrates. A custom-made oven was designed for thermal cycling and water vapor corrosion testing. The oven can test four specimens simultaneously and allows to evaluate environmental barrier performances under similar corrosion kinetics compared to turbine engines. Coatings structural evolution has been observed by SEM on the polished cross sections, and phase composition has been analyzed by XRD. All coatings have been thermally cycled between 1300 °C and the ambient temperature, without spallation, due to their porosity and the presence of additional secondary phase which increases the thermal cycling resistance. During water vapor exposure at 1200 °C, rare earth disilicates showed a good stability, which is contradictory with the literature, due to impurities—such as Si- and Al-hydroxides—in the water vapor jets. The presence of vertical cracks allowed the water vapor to reach the substrate and then to corrode it. It has been observed that thin vertical cracks induced some spallation after 24 h of corrosion.

**Keywords** environmental barrier coating (EBC) · induction thermal plasma · rare earth silicates · silicon carbide · solution precursor plasma spraying (SPPS) · thermal cycles · water vapor corrosion

## Introduction

Silicon-based ceramic composites are the leading candidates for high-temperature structural components in the next generation of gas turbine engines (Ref 1-7). Today, hot sections of engines are made of heavy cobalt- or nickel-based super alloys which have reached their operating temperature limit (about 1100 °C) (Ref 8). Replacing metal alloys by silicon-based ceramic composites, such as SiC/SiC ceramic matrix composites, would allow to increase the turbine inlet temperature up to 1500 °C and hence increase the jet engine efficiency (Ref 9). These future turbines should be lighter and more powerful and are a great innovative field of research for more environmental compliant and economical turbine propulsion systems.

One major concern is the sensitivity of Si-based ceramics to combustion environment (Ref 10-12). Indeed, the protective silica scale strongly reacts with hot water vapor to form gaseous silicon hydroxides, resulting in Si-based ceramics catastrophic erosion (about 1 µm/h in the combustion environment of commercial gas turbine engines) (Ref 13-16). A protective coating, so-called environmental barrier coating (EBC), with corrosion resistance properties at high temperatures must be applied on Si-based ceramics to preserve turbine materials from combustion environment.

Rare earth silicates are promising environmental barrier materials because they exhibit an excellent stability in high-temperature corrosive environments up to 1500 °C (Ref 17-23), they have a good chemical compatibility, and their coefficient of thermal expansion is in agreement with Si-based substrates (Ref 24, 25). Rare earth disilicates have a closer coefficient of thermal expansion with SiC/SiC composite substrate, but in presence of water vapor at high temperature, the disilicate phase decomposes into a rare

✉ Émilien Darthout  
emilien.darthout@usherbrooke.ca

<sup>1</sup> Electrochemistry, Plasmas and Energy Research Center, University of Sherbrooke, Sherbrooke, QC, Canada

earth mono-silicate phase which has a better corrosion resistance than disilicate ones (Ref 22, 26–29).

Rare earth silicate coatings were synthesized using the solution precursor plasma spray (SPPS) technique which produces nano- and submicro-structured coatings (Ref 30–33). Such coatings present enhanced performances against thermal stress compared to classical plasma spray techniques—using powders as precursors—because of the absence of large intersplat boundaries and well-dispersed porosity (Ref 34–36). The EBC application requires for coatings to withstand at temperatures as high as 1500 °C during several thousands of hours which leads to sintering. The aging of coatings produced by the SPPS process was studied in a previous paper (Ref 37). The addition of an immiscible zirconia second phase to the rare earth silicate one showed pinning effect mechanism which limited rare earth silicate grain growth compared to coatings without additional phase. Moreover, in the SPPS process, the precursor chemistry and concentration play an important role and affect the coatings microstructure (Ref 38–41). From this standpoint, a large variety of microstructures have been explored by synthesizing yttrium or lutetium silicate coatings with or without a secondary phase of zirconia.

Synthesized coatings for high-temperature applications—such as thermal barrier coatings (Ref 33, 42) or environmental barrier coatings (Ref 22, 43)—are challenging because the final product must survive at high-temperature environment but also to multiple heating and cooling cycles. The substrate/coating system forms a multilayered material, and the difference of layer's thermal expansion coefficients induces thermal stress (Ref 44). When the system is exposed to high heat flux, large thermal gradients can be generated within short times, and cracks or coating spallation arises (Ref 45). Moreover, coating material must be resistant to high-temperature corrosion in the case of environmental barrier application, and the coating structure must be hermetic to corrosive gases. Therefore, to qualify the EBC performances, coatings were subjected to thermal cycling and high-temperature corrosion tests in a custom-made oven which reproduces similar corrosion kinetics compared to turbine engines.

In the first part of this study, the custom-made oven performances have been evaluated for cycling and corrosion tests by measuring temperature evolution for thermal cycles; and by measuring the corrosion profile of bulk SiC exposed to water vapor between 1100 and 1300 °C. In the second part of this study, thermal cycling and high-temperature corrosion resistance have been evaluated for yttrium and lutetium silicate-based environmental barrier coatings synthesized by the SPPS process on SiC substrates.

## Materials and Technique

### Materials

Rare earth silicate coatings are produced using yttrium nitrate  $Y(NO_3)_3 \cdot 6H_2O$  (99.9%, Sigma-Aldrich, St. Louis, MO, USA) or lutetium nitrate  $Lu(NO_3)_3 \cdot 6H_2O$  (99.9%, Metall, Hongkong) and TEOS (tetraethyl orthosilicate)  $Si(OC_2H_5)_4$  (99.9%, Alfa Aesar, Ward Hill, MA, USA) dissolved in ethanol. Zirconium oxynitrate  $ZrO(NO_3)_2 \cdot 6H_2O$  (99.9%, Alfa Aesar, Ward Hill, MA, USA) is used as zirconium precursor. The precursor concentration is set at 10% by weight of ethanol.

Targeted and effective coating compositions are summarized in Table 1 with respect to their precursor mixture and their abbreviation used in this paper.

### Coating Deposition

The SPPS installation is represented in Fig. 1. Precursor solutions are axially injected into a Tekna PL-50 induction plasma torch (Tekna Plasma Systems Inc., Sherbrooke, QC, Canada) connected to a 3-MHz LEPEL HF power generator, by a gas blast atomizer. When injected in the high-temperature regions of the thermal plasma, the atomized solution precursor droplets undergo a rapid solvent evaporation, followed by fast pyrolysis and salt precipitation leading to the formation of solid oxide nanoparticles (Ref 46–48). These nanoparticles are exiting the plasma torch through a 25-mm converging nozzle and impinge on the SiC substrate (direct-sintered silicon carbide, UltraSiC SC-30, Coorstek, USA). Due to the expansion of the gas flow inside the low-pressure reactor, cold particles and gases are located at the periphery of the plasma jet (Ref 49). In order to prevent particles from cold regions to reach the substrate, a water-cooled metallic mask was placed between the torch and the substrate. These cold particles cannot adhere to the substrate and could introduce defects in the coating (Ref 38).

Before deposition, the SiC substrates are polished and cleaned in ultrasonic baths with ethanol during 2 min. The substrate average roughness  $R_a$  has been measured at 0.1  $\mu\text{m}$ . This low roughness tends to prevent columnar structure formation (Ref 41). Process parameters are summarized in Table 2.

Preliminary experiments showed that as-sprayed coatings, synthesized by the solution precursor plasma spraying process, are composed of a mixture of individual oxides (Ref 37) so that a high-temperature heat treatment at 1500 °C during 7 h is needed to allow the solid-state reaction between silica and rare earth oxides, resulting in the rare earth silicates formation. The coating compositions after heat treatment are summarized in Table 1.

**Table 1** Targeted and effective coating compositions and abbreviations used

Targeted composition	Abbreviation	Precursors	Effective composition (after heat treatment at 1500 °C during 7 h)
Lu <sub>2</sub> Si <sub>2</sub> O <sub>7</sub>	L	Lutetium nitrate TEOS	Lu <sub>2</sub> Si <sub>2</sub> O <sub>7</sub> ; (Lu <sub>2</sub> SiO <sub>5</sub> )
Lu <sub>2</sub> Si <sub>2</sub> O <sub>7</sub> -ZrO <sub>2</sub>	LZ	Lutetium nitrate TEOS Zirconium oxynitrate	Lu <sub>2</sub> Si <sub>2</sub> O <sub>7</sub> ; ZrO <sub>2</sub> ; (SiO <sub>2</sub> )
Y <sub>2</sub> Si <sub>2</sub> O <sub>7</sub>	Y	Yttrium nitrate TEOS	Y <sub>2</sub> SiO <sub>5</sub> ; β-Y <sub>2</sub> Si <sub>2</sub> O <sub>7</sub> ; (Y <sub>2</sub> O <sub>3</sub> )
Y <sub>2</sub> Si <sub>2</sub> O <sub>7</sub> -ZrO <sub>2</sub>	YZ	Yttrium nitrate TEOS Zirconium oxynitrate	β-Y <sub>2</sub> Si <sub>2</sub> O <sub>7</sub> ; ZrO <sub>2</sub> ; (SiO <sub>2</sub> )

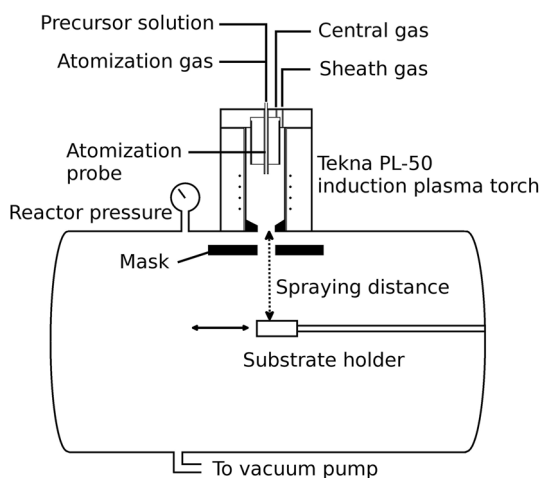


**Fig. 1** Schematic illustration of the induction plasma process for coating deposition

**Table 2** SPSS process parameters

Parameter	Value
Plate power	42 kW
Central gas (Ar)	23 slpm
Sheath gas (O <sub>2</sub> )	63 slpm
Atomization gas (Ar)	12 slpm
Reactor pressure	10.7 kPa
Precursor solution flow	10 mL/min
Precursor solution concentration	10 wt.%
Spraying distance	100 mm
Sample holder speed	5 cm/s
Preheating cycles	10
Deposition cycles	40

**Custom-Made Oven Design and Testing Protocols**

The custom-made oven can perform thermal cycling and high-temperature corrosion tests (see Fig. 2). The heating

module is a Superthal muffle module (Kanthal, Sweden) able to reach 1500 °C in vertical position. The heating module is supported and covered by MgO refractories with additional mullite fiber papers (Fiberfrax Paper 1600, Unifrax, Tonawanda, NY, USA) on top to ensure an optimal thermal insulation (not represented in Fig. 2). Four specimens are mounted simultaneously on a sample holder made of high purity mullite foam (Fiberfrax Duraboard 1800R, Unifrax, Tonawanda, NY, USA) placed on a mullite tube which exhibits a strong thermal shock resistance.

In thermal cycle configuration, the sample holder could be raised into the high-temperature oven by a programmable pneumatic cylinder. When the sample holder is at its low position—outside the oven—a cold air jet can increase the cooling rate. A type-R thermocouple measures the temperature of the substrate holder near its support surface, and +45 and −55 °C/s were, respectively, recorded as maximum heating and cooling rates. Samples underwent 5 cycles of 50 min at 1300 °C and 10 min at ambient temperature with forced cold air jet. Figure 3 shows the temperature evolution curve during a thermal cycle test. Due to thermal mass, 4 min were required to reach 1300 °C starting from room temperature when samples were introduced inside the oven, and less than 2 min to cool them down to 200 °C with the cold air jet.

In corrosion configuration, the oven is set up with four mullite tubes with 1.6 mm internal diameter which were added on the top of the oven to allow room-temperature water injection. The position of the sample holder in the oven was lowered in order to extend the exposition of water tubes to high-temperature environment to allow for a good heat transfer to the water vapor-fed in the four tubes. Indeed, liquid water evaporates in the tubes and produces superheated steam which is ejected 1 cm above each sample. The water is channeled to each tube separately by a medical I.V. bag which contains a reserve of ultra-pure water at room temperature. The water flow is regulated at 0.75 mL/min on each tube using a sight chamber and a roll

**Fig. 2** Schematic cross sections of the custom oven in heating position in thermal cycling configuration (left) and high-temperature water–vapor corrosion configuration with four water injection tubes (right)

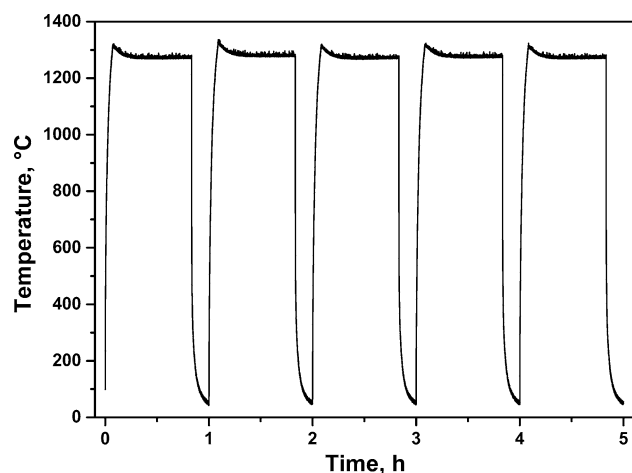
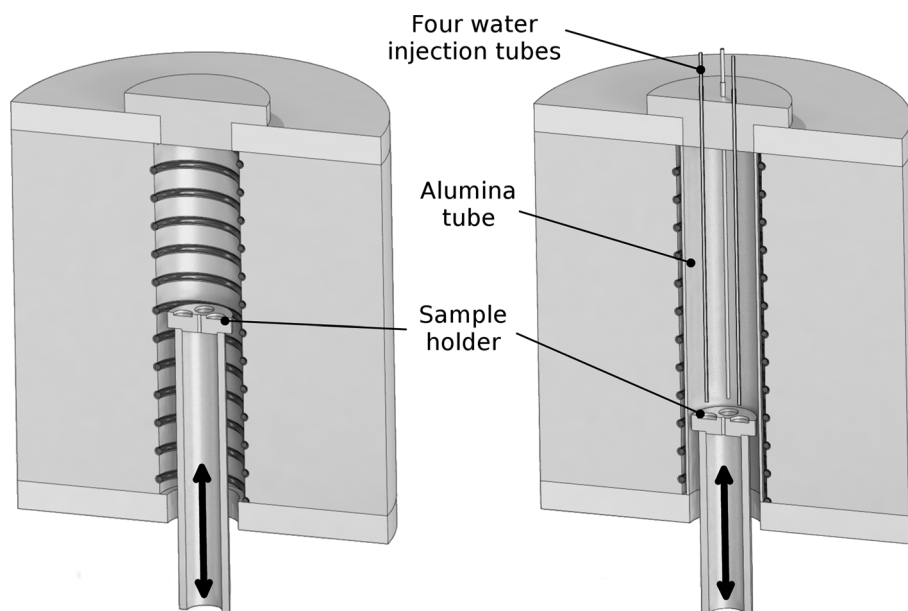


**Fig. 3** Temperature evolution curve during the thermal cycles at 1300 °C for 50 and 10 min cooling

clamp. The water vapor jet velocity  $v$  is estimated using the ideal gas law:

$$v = \frac{\dot{m}RT}{AM_w P} \quad (\text{Eq 1})$$

where  $\dot{m}$  is the mass flow rate,  $R$  the universal gas constant,  $T$  the temperature of the jet,  $A$  the cross-sectional area of the injection tube,  $M_w$  the molecular weight of water, and  $P$  the pressure at the exit of the injection tube. Therefore, samples are exposed to high-temperature water vapor flow during 24 h at temperature between 1100 and 1300 °C with corresponding gas velocity between 39 and 45 m/s.

### Characterization Techniques

High-temperature corrosion performance has been evaluated by exposing SiC substrates to the steam jet, and resulting corrosion profiles have been measured with a mechanical profilometer on a Dektak 150 Surface Profiler (Veeco, NJ, USA). Each corroded substrate has been scanned during 60 s, with a 10-mg stylus force (vertical resolution of 10 Å), on a 2 × 12 mm surface with 10 lines scan. The numerical scans were smoothed by a surface fitting algorithm (Ref 50) to rebuild the corrosion crater surfaces in 3D. The maximum recession depth is then measured from the numerically rebuilt surface, and the experimental SiC recession rate is then estimated in μm/h.

Phase compositions of environmental barrier coatings have been analyzed by X-ray diffraction (XRD) on a Philips X'Pert Pro MPD X-ray diffractometer (Eindhoven, Netherlands) using CuK $\alpha$  radiation source. The phase identification was done according to JCPDS cards 30-1468 for yttrium-stabilized cubic ZrO<sub>2</sub>, 74-7393 for cubic Y<sub>2</sub>O<sub>3</sub>, 12-4410 for  $\beta$ -Y<sub>2</sub>Si<sub>2</sub>O<sub>7</sub>, 07-4730 for X<sub>2</sub>-Y<sub>2</sub>SiO<sub>5</sub>, 35-0326 for Lu<sub>2</sub>Si<sub>2</sub>O<sub>7</sub>, 230-0212 for Lu<sub>2</sub>SiO<sub>5</sub> and 73-1370 for cubic YAG (Y<sub>3</sub>Al<sub>5</sub>O<sub>12</sub>).

Coating microstructure observations were performed on a Hitachi S-4700 field emission scanning electron microscope (Tokyo, Japan). Beforehand, samples were fractured and mounted in epoxy resin to obtain polished cross sections.

## Results and Discussion

### Corrosion Performances Qualification

Figure 4 shows the corrosion test results where four SiC pellets have been simultaneously exposed to water vapor jets at 1100, 1200, and 1300 °C during 24 h. At 1200 °C, SiC recession rates were measured at 1.33 μm/h which is typical for turbine engines under standard combustion conditions (Ref 12, 13, 51, 52).

The recession of SiO<sub>2</sub> formers under gas flow containing water vapor is due to the formation of volatile species—mostly Si(OH)<sub>4</sub> (Ref 53)—at the outer surface by a reaction between silica and water vapor. The corrosion kinetic is limited by the transport of Si(OH)<sub>4</sub> through the boundary layer. The molar flux *J* (in mol/(cm<sup>2</sup>.s)) of the corrosion product Si(OH)<sub>4</sub> by convective mass transfer is calculated using (Ref 54):

$$J = 0.664 \left( \frac{Lv\rho}{\eta} \right)^{1/2} \left( \frac{\eta}{D\rho} \right)^{1/3} \frac{D\rho_V}{L} \quad (\text{Eq 2})$$

with *L* is the mullite tube internal diameter (0.16 cm), *v* the gas velocity (3.9 × 10<sup>3</sup> cm/s at 1100 °C), *ρ* the steam density (1.58 × 10<sup>-4</sup> g/cm<sup>3</sup> at 1100 °C), *η* the dynamic viscosity of the steam (4.281 × 10<sup>-4</sup> g/(cm.s) at 1100 °C (Ref 55)), *D* the interdiffusion coefficients of Si(OH)<sub>4</sub> into steam at 1100 °C (1.91 cm<sup>2</sup>/s) and *ρ<sub>v</sub>*, the Si(OH)<sub>4</sub> molar density at the solid surface (2.59 × 10<sup>-11</sup> mol/cm<sup>3</sup> at 1100 °C). The interdiffusion coefficient has been estimated using Lennard-Jones potential (SiF<sub>4</sub> approximates Si(OH)<sub>4</sub>) (Ref 54, 55) and the Hirschfelder, Bird and Spatz equation (Ref 56). The Si(OH)<sub>4</sub> density at 1100 °C under 1 atm at the surface

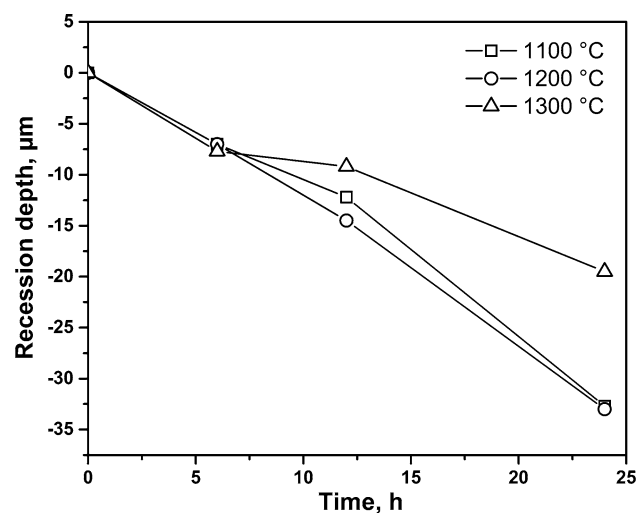


Fig. 4 Experimental measurements of recession depth of SiC corrosion vs. duration of exposition to water vapor at different temperature

corresponds to the equilibrium density of Si(OH)<sub>4</sub> considering the reaction between SiO<sub>2</sub> and water vapor which has been found in the literature from experimental and theoretical work (Ref 53, 57-59). Moreover, Si(OH)<sub>4</sub> is considered as the only product of reaction between silica and water vapor, so that the Si(OH)<sub>4</sub> molar flux *J* is directly linked to SiC recession rate *y* (in μm/h) according to:

$$y = \frac{J \times M_w(\text{SiC}) \times 3.6 \times 10^7}{\rho(\text{SiC})} \quad (\text{Eq 3})$$

with *M<sub>w</sub>(SiC)* the molecular weight of silicon carbide (40.11 g/mol) and *ρ(SiC)* the silicon carbide density (3.21 g/cm<sup>3</sup>). Therefore, Eq 2 gives a Si(OH)<sub>4</sub> molar flux of 2.81 × 10<sup>-9</sup> mol/(cm<sup>2</sup>.s) and Eq 3 gives the SiC recession rate equal to 1.54 μm/h. This theoretical estimation agrees with the SiC recession rate of 1.29 μm/h, measured during our experiments at 1100 °C. The same order of magnitude has been observed for the recession rates on bulk materials—such as SiO<sub>2</sub> and SiC—in the literature using the same type of steam-jet furnace (Ref 60, 61). Table 3 summarizes measured and estimated SiC recession rates between 1100 and 1300 °C from this study and other recession rates from the literature.

In this study, the measured and calculated SiC recession rates at 1100 °C are in good agreement. On the contrary, the measured SiC recession rate at 1300 °C is more than three times lower than the calculated one. This behavior is explained by the Leidenfrost effect inside the mullite tubes. A mullite tube has an inlet part outside the oven (at room temperature) and its outlet part inside the oven (at high temperature). As the water flow rate is low and constant, it could be considered that, inside the tube, the water flow is laminar (Reynolds number *Re* ≪ 1) with a constant linear velocity of 6.3 mm/s. The vaporization zone, i.e., where the phase change occurs, begins just before the water enters inside the oven and spreads over 10 mm long. This zone is easily identified a posteriori because impurities (salts) are liberated when water vaporizes and leaves a characteristic yellow color. Therefore, when the water flows along the tube, the internal tube temperature rises rapidly above the saturation temperature and boiling takes place. According to the typical boiling curve of water, there are several boiling regimes depending on the excess temperature: the difference between the temperature of the internal tube temperature and the saturation temperature of the fluid. When the oven internal temperature is set to 1100 °C, the thermal gradient is moderate so that nucleate boiling regime takes place and heat transfer between tube wall and water is optimal, resulting in complete water vaporization. When the oven temperature increases up to 1300 °C, thermal gradient increases as well, so that transition regime takes place before the complete water vaporization. This implies that heat transfer is degraded until the Leidenfrost point, and the

**Table 3** Experimental and theoretical recession rates of SiC and SiO<sub>2</sub> (*T* the temperature, P(H<sub>2</sub>O) the partial pressure of water and *v* the gas velocity)

Reference	Material	Experimental conditions	Measured SiC recession rates, μm/h	Calculated SiC recession rates, μm/h
This study	SiC	<i>T</i> = 1100 °C P(H <sub>2</sub> O) = 1 atm <i>v</i> = 39 m/s	1.29	1.54
		<i>T</i> = 1200 °C P(H <sub>2</sub> O) = 1 atm <i>v</i> = 42 m/s	1.33	2.19
		<i>T</i> = 1300 °C P(H <sub>2</sub> O) = 1 atm <i>v</i> = 45 m/s	0.83	3.08
Lucato et al. (Ref 61)	SiC	<i>T</i> = 1160 °C P(H <sub>2</sub> O) = 1 atm <i>v</i> = 260 m/s	0.5-0.8	n/a
		<i>T</i> = 1350 °C P(H <sub>2</sub> O) = 1 atm <i>v</i> = 160 m/s	0.6-0.7	n/a
Golden and Opila (Ref 60)	SiO <sub>2</sub>	<i>T</i> = 1300 °C P(H <sub>2</sub> O) = 1 atm <i>v</i> = 172 m/s	2.3*	n/a

\* This value has been converted from SiO<sub>2</sub> recession rate

remaining liquid water is then surrounded by a steam film which prevents the water droplets to receive enough heat to vaporize and transports the water droplets outside the tube. When the oven internal temperature was set to 1300 °C, this droplet spray has been observed experimentally by placing a mirror at the bottom exit of the oven when water is injected in the four tubes. During corrosion tests, it leads to sample surface cooling which drastically decreases the SiC recession rate. Moreover, using Eq 2 and 3, a SiC recession rate of 0.8 μm/h is predicted for a temperature of 1000 °C, which confirms the cooling effect of the droplet spray. Setting up the oven temperature at 1100 and 1200 °C, no droplet spray has been observed.

In addition, corrosion replication tests have been realized on SiC at 1200 °C during 24 h. Four samples were placed on the sample holder to verify that all four injection tubes generate water vapor with similar properties. Profilometer measurements showed a recession depth with a mean value of  $33 \pm 3$  μm for the four samples which confirms that all injection tubes are similar and the simultaneous four corrosion tests are reproducible.

## Thermal Cycling Tests

### Sources of Thermal Stress

As described in the literature (Ref 62), stresses in coatings could be classified in different categories: intrinsic stresses

and thermal stresses. Intrinsic stresses arise during the deposition process (mentioned as deposition stress) and/or heat treatments (mentioned as isothermal exposure stress) which include grain growth or sintering mechanisms.

At first, deposition stress occurs during the deposition process and originates from primary cooling (quenching stress of particles impinging the substrate) and secondary cooling (cooling to room temperature of the coating/substrate system after the deposition). These deposition stresses could lead to the emergence of tensile stress in the coating and thus cracking or spallation. After deposition, samples were placed 1 min in an ultrasonic bath to remove non-adherent particles because of the primary cooling and no weight loss (under 1%) was recorded.

After the deposition process, samples were heat-treated during 7 h at 1500 °C in order to form silicate phases (see SEM micrographs in Fig. 5). Isothermal stresses could develop, while sintering occurs in the coating due to the submicronic structure of as-sprayed coatings and the solid-state reactions. Grain coarsening and densification are conjugated phenomenon which takes place during sintering. A previous study (Ref 37) highlighted that the presence of a silica phase induces a viscous sintering which results in an important densification and thus tensile stresses in YZ and LZ coatings. The densification mechanism, linked to viscous sintering, leads to the large vertical crack formation (segmentation cracks) from stress relaxation as illustrated in Fig. 2, 3, 4, and 5.

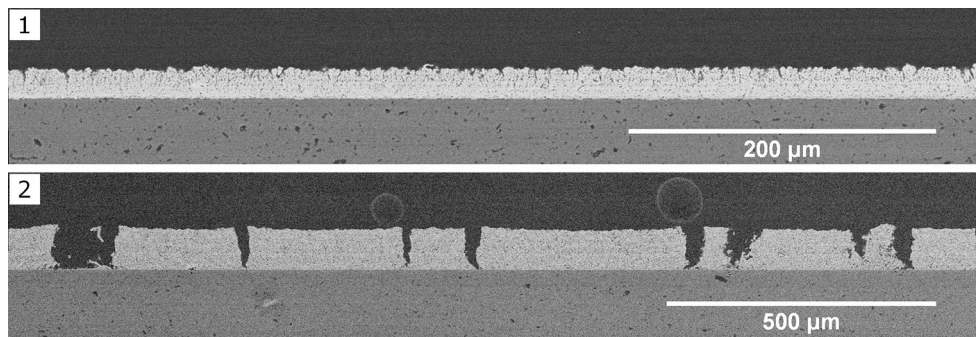


**Fig. 5** SEM micrographs after heat treatment at 1500 °C during 7 h; (1)  $\text{Y}_2\text{Si}_2\text{O}_7$  coating (no densification) and (2)  $\text{Y}_2\text{Si}_2\text{O}_7\text{-ZrO}_2$  with segmentation cracks resulting from densification, after (37)

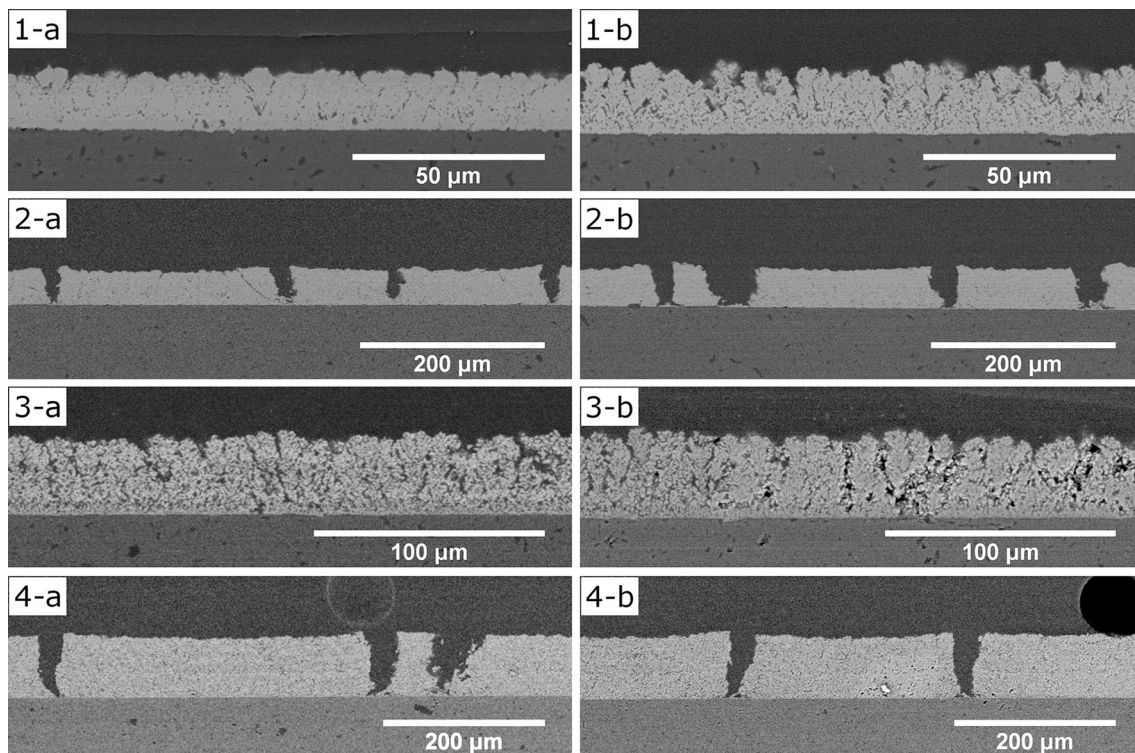


**Fig. 6** Representative BSE-SEM micrographs of L (1), LZ (2), Y (3) and YZ (4) heat-treated coatings before (a) and after (b) thermal cycling test

Therefore, after the heat treatment, the silicate phases are formed and the coating microstructure is stabilized so that, at this stage, the coating is supposed in a reference state for thermal cycling tests.

#### *Thermal Cycling Resistance of Coatings*

SEM micrographs of thermal cycling tested samples in air are displayed in Fig. 6 with their references for comparison. No macroscopic spallation has been noticed on any coatings after thermal cycling tests. Indeed, lutetium and yttrium silicate materials have been chosen for their

coefficient of thermal expansion in agreement with the substrate (see Table 4) as well as for their good thermal cycling resistance. Therefore, the thermal cycling tests validate the yttrium and lutetium silicates choice as environmental barrier coating material regarding their thermal cycling resistance properties. Moreover, the porous structure and vertical cracks promote the coating resistance to thermal cycling tests.

The major phase of L coatings is the lutetium disilicate  $\text{Lu}_2\text{Si}_2\text{O}_7$  with additional traces of lutetium mono-silicate  $\text{Lu}_2\text{SiO}_5$ , due to a lack of silica during the deposition process. The mono-silicate phase is reduced to traces so

that L coatings composition can be considered as homogeneous and as a result no thermal stress can be generated from composition variation.

Y coatings are composed of two main phases: yttrium mono-silicate  $Y_2SiO_5$  and yttrium disilicate  $\beta$ - $Y_2Si_2O_7$ . The mono-silicate phase has a CTE twice higher than the disilicate phase (see Table 4) which induces tensile stress upon cooling. This thermal stress arises for the first time during the heat treatment cooling step when the temperature drops from 1500 °C to ambient temperature in the oven at a rate of 7 °C/min. After the Y coating was thermally cycled following Fig. 3 thermal evolution, no additional damage is observed which confirms that the porosity structure renders the coating compliant to tensile stresses by decreasing the apparent elastic modulus (Ref 63).

For LZ and YZ coatings, the secondary phase of stabilized zirconia has a CTE three times higher than rare earth silicates which could induce thermal stresses. The zirconia grains addition affects the yttrium or lutetium silicate grains morphology (see Fig. 7) and gives to these silicate grains a more circular shape by pinning effect (Ref 37). Therefore, the grain boundaries are homogeneously distributed which favors a homogeneous distribution of thermal stresses. LZ and YZ coatings have also a third silica ( $\beta$ -cristobalite) phase identified by XRD. As-sprayed LZ and YZ coatings show an amorphous silica excess which

crystallizes during the heat treatment at 1500 °C in  $\beta$ -cristobalite. During the heat treatment cooling step, the  $\beta$ -cristobalite phase transforms into  $\alpha$ -cristobalite at 200 °C and this phase transformation is displacive with a volume contraction about 4% (Ref 64, 65). Therefore, additional tensile stress arises in the coating at 200 °C due to the  $\beta$ -to- $\alpha$  cristobalite transformation. The inverse transformation  $\alpha$ -to- $\beta$  occurs at 300 °C during the next heating step which is accompanied by the inverse volume expansion. Breneman et al. (Ref 66) studied the hysteresis on  $\alpha$ - $\beta$  transition temperature when a cristobalite powder is subjected to repeated thermal cycles. They observed that cristobalite grains with a diameter inferior to 38  $\mu$ m did not show hysteresis. They explain this phenomenon by microcracks appearing in large cristobalite grains and not in grains smaller than 38  $\mu$ m. In YZ and LZ coatings, the cristobalite grains have a diameter around 2  $\mu$ m (see (Ref 37)), so that these grains can certainly accommodate tensile stresses developing during the repeated thermal cycling tests so that coating spallation can be avoided.

All coatings present a cristobalite interphase between the coating and the substrate (see Fig. 8) which is induced at high temperature by oxygen migration through the coating pores resulting in substrate oxidation (Ref 67, 68). This thermally grown oxide (TGO) layer of cristobalite is subjected to tensile stress during cooling due to the above-mentioned  $\beta$ -to- $\alpha$  cristobalite displacive transformation. Based on experimental results, Richards et al. (Ref 69) proposed a delamination mechanism of an EBC system which develops a similar silica TGO layer. After exposing their tri-layer EBC system (Si/mullite/ $Yb_2SiO_5$ ) to thermal cycling and water vapor environment at 1316 °C, they observed that the TGO layer with a thickness higher than 10  $\mu$ m causes the EBC delamination by microcracking (due to cristobalite  $\alpha$ - $\beta$  transformation). After Richards et al., this cristobalite TGO layer is considered as the major weakness of the EBC systems. In our experiments, no EBC delamination has been observed after thermal cycling tests

**Table 4** Coefficient of thermal expansion (CTE) of bulk materials (Ref 26, 42, 81–84)

Material	CTE ( $10^{-6} K^{-1}$ )
$Lu_2Si_2O_7$	3.84
$\beta$ - $Y_2Si_2O_7$	3.9
$Y_2SiO_5$	8.4
Stabilized $ZrO_2$	9–11
$\alpha$ -cristobalite	9.5
$\beta$ -cristobalite	4.5
SiC	3.8

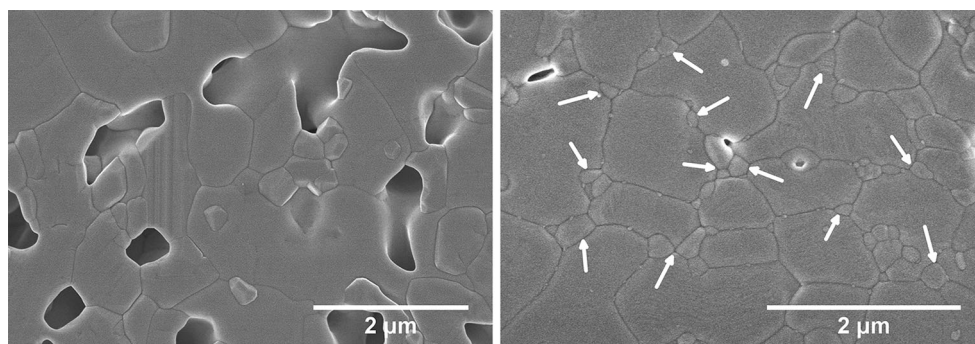


**Fig. 7** SEM micrographs of heat-treated  $Y_2Si_2O_7$  (left) and  $Y_2Si_2O_7$  with additional  $ZrO_2$  (right) coatings (zirconia grains indicated by white arrows)



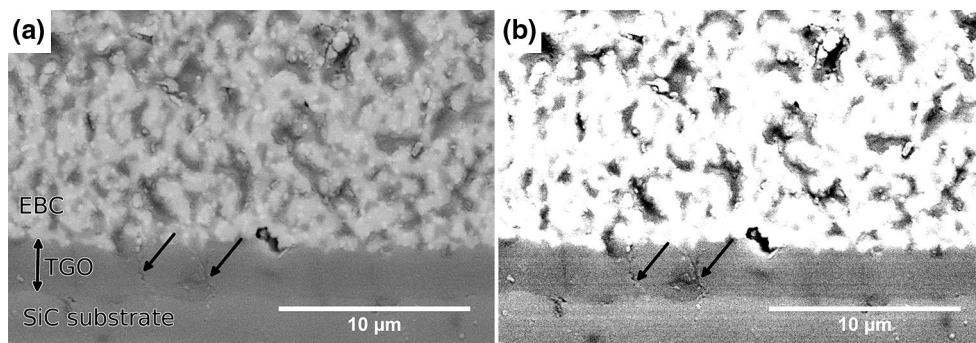


**Fig. 8** (a) BSE-SEM micrograph of YZ coating after thermal cycling test showing cristobalite TGO layer (2.7  $\mu\text{m}$  thick) with isolated microcracks indicated by black arrows (b) enhanced phase contrasts

of the same micrograph highlighting the vertical microcracks and the TGO layer

despite the presence of a cristobalite TGO layer. Indeed, Fig. 8 shows the presence of isolated microcracks in the TGO layer, but the TGO layer is thin enough (under 3  $\mu\text{m}$ ) to avoid catastrophic delamination during thermal cycling tests.

### High-temperature Corrosion Tests

#### *EBC Performances Under High-Temperature Water Vapor Exposure*

Figure 9 displays BSE-SEM micrographs of coating cross sections after water vapor exposure at 1200  $^{\circ}\text{C}$  during 24 h. The four water vapor jets were directed normally to the four samples center, and the coating spallation occurs at the impingement points of the water vapor jets. The SEM observations in Fig. 10 were made at the edge of the spallation zone in order to illustrate the integrity of the remaining coating.

After heat treatment in air at 1500  $^{\circ}\text{C}$  during 7 h, the TGO layer has an average thickness inferior to 1  $\mu\text{m}$ , see Fig. 10. After corrosion tests, the TGO thickness has increased and measurements are reported in Table 5. According to Richards et al. (Ref 22), the TGO thickness growth is driven by oxygen diffusion through  $\text{Yb}_2\text{Si}_2\text{O}_7$  and has been estimated at 1.44 nm/h for a 100- $\mu\text{m}$ -thick dense coating when exposed to 90% vol.  $\text{H}_2\text{O}$  and 10% vol.  $\text{O}_2$  atmosphere at 1316  $^{\circ}\text{C}$ . From our results summarized in Table 5, the TGO thickness growth rate has been measured between 100 and 150 nm/h which represents a value 100 times higher than Richards' one. Therefore, this suggests that oxidizer transport is much faster than molecular diffusion. Indeed, the water vapor can migrate through coatings porosity which provides a direct pathway for oxidizer to the substrate. Moreover, according to the discussion on section “Sources of Thermal Stress”, the TGO thickness has to be controlled and minimized in order to prevent spallation during thermal cycles.

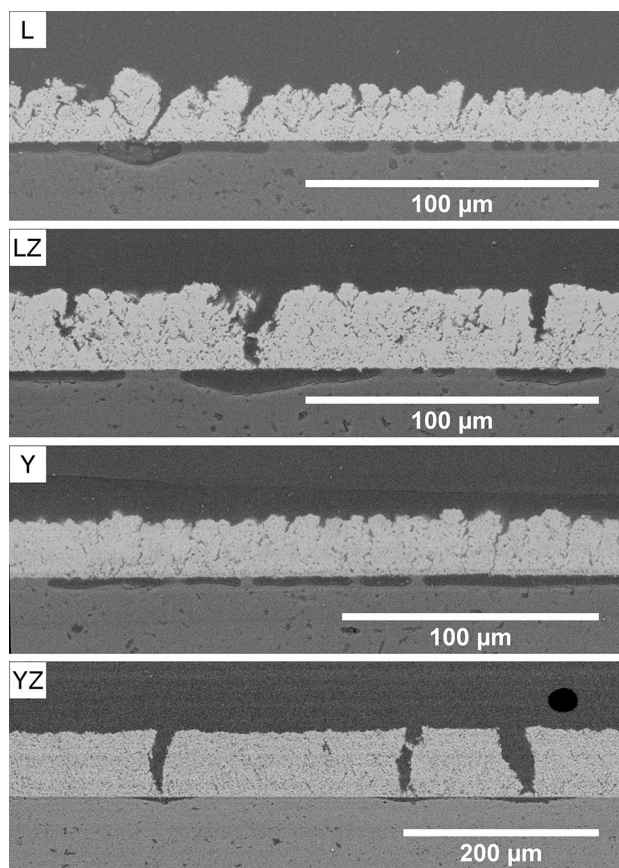


**Fig. 9** Representative BSE-SEM micrographs of L, LZ, Y and YZ coatings after corrosion tests (24 h at 1200  $^{\circ}\text{C}$  and 1 atm-100%  $\text{H}_2\text{O}$ )

Through-coating cracks provide another direct pathway for water vapor to the SiC substrate and cause substrate oxidation and recession. The SiC oxidation and silica volatilization reactions occur simultaneously and are described by parabolic kinetics (Ref 13). The parameter dependence derived from the parabolic model of SiC oxidation and silica volatilization explains both morphology of corrosion voids created on SiC substrate observed in Fig. 9 and reproduced in Fig. 11.

Figure 11 shows two representative corrosion voids: the first is characterized by thin cracks and a thin corrosion void along the silica interphase, and the second is characterized by large cracks and a deep corrosion void located at the bottom of the crack. The main difference between both types of corrosion voids is the limiting oxide thickness  $x_L$ , expressed by derivation from the parabolic model (Ref 13, 70):

$$x_L = \frac{k_p}{2k_l} \quad (\text{Eq 4})$$

where  $k_p$  and  $k_l$  are SiC oxidation parabolic rate constant and SiC volatilization linear rate constant, respectively. This limiting oxide thickness is the thickness of the silica scale between the corrosive environment and the SiC substrate. It results from the competition between SiC oxidation and silica volatilization reactions. In the case of the thin cracks (Fig. 11a), the limiting oxide scale is visible and is approximately 1  $\mu\text{m}$  thick. Considering that the steady state is achieved, the presence of this limiting oxide thickness confirms the parabolic kinetic of oxidation/volatilization and suggests that both reactions are taking place. In the case of large cracks (Fig. 11b), this oxide scale is not visible at the bottom of the void—as in pure SiC oxidation preliminary experiments (section “Corrosion performances qualification”)—and it is supposed too thin to appear on SEM micrographs at  $\times 5000$  magnification with backscattering electron detector. The « absence » of oxide scale is an indication of the predominance of the volatilization over the oxidation reaction. Considering the volatilization reaction limited by product transport, large cracks allow a rapid extraction of the volatile by-products by convection which results in enhanced corrosion

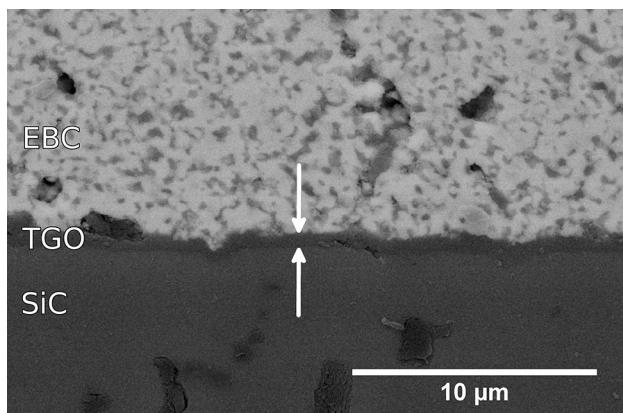


**Fig. 10** BSE-SEM micrograph of LZ coating reference (after the heat treatment at 1500 °C during 7 h) showing the TGO layer of  $0.7 \pm 0.1 \mu\text{m}$

**Table 5** Morphological characteristics of L, LZ, Y and YZ coatings after 24 h at 1200 °C in water vapor atmosphere

Coating	Thickness, $\mu\text{m}$		Spallation percentage, %	TGO thickness, $\mu\text{m}$	
	Before	After		Before	After
L	$17.5 \pm 1.1$	$17.6 \pm 0.9$	1.7	$0.4 \pm 0.1$	$3.9 \pm 0.2$
LZ	$28.7 \pm 1.1$	$27.4 \pm 1.0$	1.1	$0.7 \pm 0.1$	$3.1 \pm 0.2$
Y	$21.5 \pm 0.8$	$22.1 \pm 1.1$	0	$0.5 \pm 0.1$	$4.0 \pm 0.6$
YZ*	$73.2 \pm 2.1$	n/a	19.6	$0.6 \pm 0.1$	n/a

\* EBC layer was spalled off under the water vapor injection point

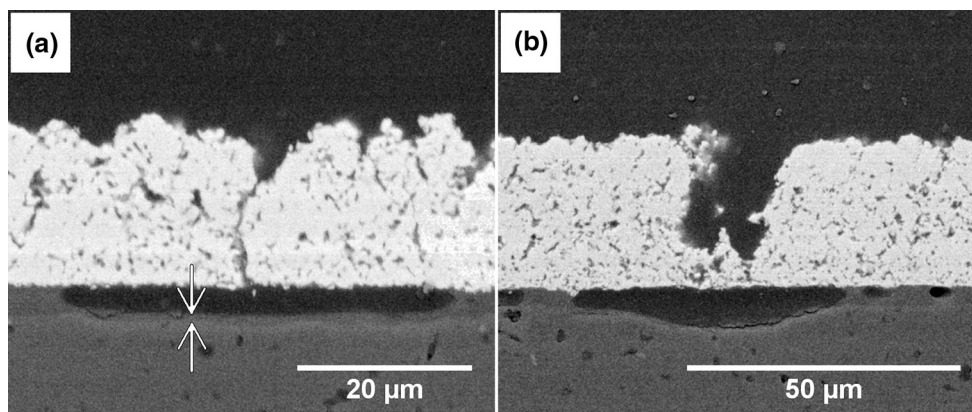


**Fig. 11** BSE-SEM micrographs of coatings after corrosion test showing corrosion voids and cracks; (a) L coating with thin crack and  $\text{SiO}_2$  layer is highlighted between the arrows; (b) LZ coating with large crack

compared to thin cracks where mass transport is achieved by diffusion. Therefore, the corrosion voids morphology is related to the crack width.

Moreover, the vertical crack width is correlated with the EBC spallation percentage after the corrosion test (see Table 5). Y coating shows only a few thin cracks, and, after 24 h at 1200 °C in 100% water vapor atmosphere, the coating has no spallation and only few TGO corrosion spots. L and LZ coatings have more numerous thin cracks which lead to a more rapid TGO corrosion. The spallation percentage is under 2% after the corrosion test. YZ coating has the largest vertical cracks which induce catastrophic spallation under water vapor action. This is explained by the ease for water vapor to reach the substrate and the TGO. As the silica volatilization reaction has a fast kinetic, the TGO is corroded which induces the rapid coating spallation. In fact, as demonstrated by Richards et al., the corrosion of the TGO reduces drastically the EBC lifetime when exposed to water vapor at high temperature (Ref 69). Indeed, the presence of vertical cracks in our coatings provides a direct access for water vapor to the TGO which is easily corroded. As the TGO corrosion induces rapid coating spallation, the EBC ideal design should be a dense—or at least water–vapor hermetic—coating (Ref 71).

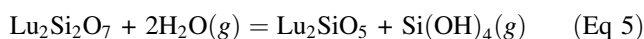
#### Recession of Coating Materials

Bulk rare earth silicates have demonstrated their resistance to water vapor corrosion at high temperature in the literature (Ref 22–26, 29, 69, 72–74). Table 5 contains the coating thickness measurements before and after corrosion tests and their spallation percentage. As expected, all coating materials showed an excellent resistance to water vapor corrosion with no thickness decrease after SEM measurements. Indeed, according to the literature, the erosion rate of rare earth silicates is estimated between 1 to 10 nm/h when exposed to high-temperature water vapor environments (Ref 17, 24, 75) which indicates that after our 24-h corrosion tests, the thickness of our coatings should have decreased about 200 nm, which is not measurable on our SEM micrographs.

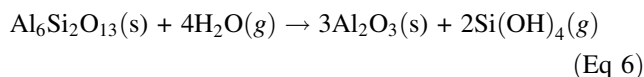
Macroscopic corrosion damages are observed from the coating spallation which are caused by the corrosion of the silica TGO layer as demonstrated in the previous section. L and Y coatings show a low spallation—even no spallation for Y coating—due to the presence of thin cracks which limit water vapor access to the TGO layer and the SiC substrate. LZ coating also shows a low spallation because large cracks are present but not predominant. Nevertheless, the YZ coating only exhibits large cracks with an average aperture of 20 μm, which does not provide an efficient barrier to water vapor, resulting in its fast coating spallation.

The chemical stability of the coatings was also analyzed by XRD after corrosion tests. Rare earth silicates are known to be corrosion resistant but they react—at very low constant rates of reaction—with water vapor. Figure 12 shows XRD patterns of L, LZ, Y and YZ coatings before and after the water vapor corrosion tests.

**L Coating** L coating is composed of a Lu<sub>2</sub>Si<sub>2</sub>O<sub>7</sub> major phase and a Lu<sub>2</sub>SiO<sub>5</sub> minor phase before corrosion tests. After corrosion, Lu<sub>2</sub>Si<sub>2</sub>O<sub>7</sub> phase is still the major phase, while Lu<sub>2</sub>SiO<sub>5</sub> content is reduced to traces. Ueno et al. found that, at 1300 °C, Lu<sub>2</sub>Si<sub>2</sub>O<sub>7</sub> dissociates into Lu<sub>2</sub>SiO<sub>5</sub> under the water vapor action following (Ref 28):



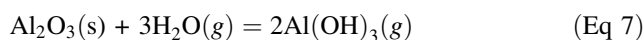
In our case, the Lu<sub>2</sub>Si<sub>2</sub>O<sub>7</sub> dissociation is not observed. An explanation could be found considering the mullite tubes which are used to bring the water vapor to the tested samples. It is well known that mullite reacts with water vapor according to the equation (Ref 76):



Our water vapor jet is then charged with silicon hydroxide which modifies the chemical equilibrium of reaction presented in Eq. 5. This could inhibit the chemical reaction between Lu<sub>2</sub>Si<sub>2</sub>O<sub>7</sub> and water vapor and favor the reverse reaction between silicon hydroxide and Lu<sub>2</sub>SiO<sub>5</sub> which leads to the formation of Lu<sub>2</sub>Si<sub>2</sub>O<sub>7</sub>. This could explain the decrease of the relative amount of the Lu<sub>2</sub>SiO<sub>5</sub> phase after the corrosion test.

**LZ Coating** Before the corrosion test, the LZ coating was composed of Lu<sub>2</sub>Si<sub>2</sub>O<sub>7</sub> and ZrO<sub>2</sub> with an excess of SiO<sub>2</sub>. As expected, after corrosion test, the SiO<sub>2</sub> phase has been vaporized into silicon hydroxide and Lu<sub>2</sub>Si<sub>2</sub>O<sub>7</sub> and ZrO<sub>2</sub> stays stable. The stability of Lu<sub>2</sub>Si<sub>2</sub>O<sub>7</sub> at 1200 °C has already been observed in the L coating, and ZrO<sub>2</sub> is known for its strong water vapor corrosion resistance (Ref 77).

**Y Coating** Before corrosion test, the Y coating was composed of Y<sub>2</sub>SiO<sub>5</sub> major phase, Y<sub>2</sub>Si<sub>2</sub>O<sub>7</sub> secondary phase and Y<sub>2</sub>O<sub>3</sub> traces which remains because of a lack of silica input during the deposition process. After corrosion test, a YAG (Y<sub>3</sub>Al<sub>5</sub>O<sub>12</sub>) phase has been identified on XRD analysis (see Fig. 12). The aluminum could come from the mullite tubes, which have on their surface an alumina phase after Eq. 6, and the alumina tube (see Fig. 2). The reaction between water vapor and alumina produces a gaseous aluminum hydroxide Al(OH)<sub>3</sub> according to the equation (Ref 78):



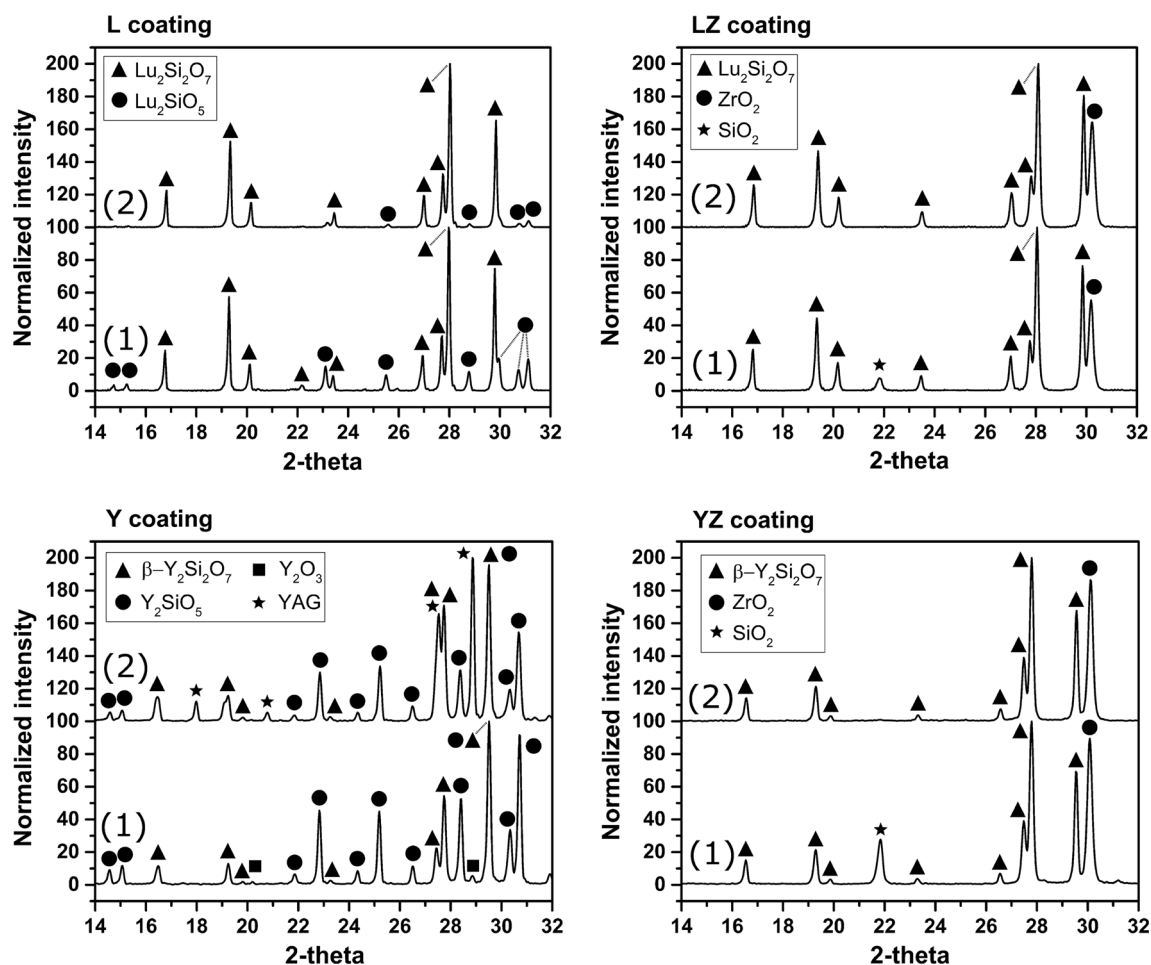


**Fig. 12** XRD analysis of L, LZ, Y and YZ coatings before (1) and after (2) corrosion tests at 1200 °C during 24 h

The equilibrium partial pressure of the aluminum hydroxide in 1 atm.  $\text{H}_2\text{O}$  environment at 1400 °C is one order magnitude lower than the silicon hydroxide one (Ref 78, 79). This indicates that this reaction is not preponderant but non-negligible. This results in the formation of YAG phase in the presence of yttrium oxide or yttrium monosilicate. Similar rare earth aluminum garnet formation on rare earth (Y, Yb, Lu) silicate coatings has been observed during water vapor corrosion experiments by Maier et al. (Ref 19). Moreover, comparing the relative peak intensities of  $\text{Y}_2\text{Si}_2\text{O}_7$  and  $\text{Y}_2\text{SiO}_5$  phase, the  $\text{Y}_2\text{Si}_2\text{O}_7$  amount has increased after the corrosion test. This behavior has already been observed for L coatings where the mono-silicate phase reacts with the Si-hydroxide, contained in the water vapor, to form a disilicate phase.

**YZ Coating** Before the corrosion test, the YZ coating was composed of  $\text{Y}_2\text{Si}_2\text{O}_7$  and  $\text{ZrO}_2$  with an excess of  $\text{SiO}_2$ . After the corrosion test, the  $\text{Y}_2\text{Si}_2\text{O}_7$  and  $\text{ZrO}_2$  phases

remain stable, while the cristobalite was corroded away by water vapor.

These results demonstrate that the partial pressure of Si- and Al-hydroxides in the water vapor jet has an incidence on the environmental barrier surface composition. When the literature results show that rare earth disilicates tend to decompose into mono-silicates (Ref 22, 24, 26, 28, 80), we observed that this reaction equilibrium has been displaced due to the presence of Si-hydroxide in our corrosive gases.

## Conclusion

The custom-made oven has demonstrated its capabilities in terms of thermal cycling and high-temperature corrosion. With +45 and  $-55$  °C/s, as, respectively, heating and cooling rates, thermal cycling experiments are efficient to test the mechanical behavior of coating/substrate systems under high thermal gradients. Bulk SiC corrosion experiments show recession rates of about 1  $\mu\text{m}/\text{h}$  at 1200 °C in a

saturated water vapor atmosphere which is close to recession rates observed in industrial turbines under service conditions.

Coatings have been successfully thermal cycled and have withstood thermal cycles without delamination. Their porous structure increases their damage resistance to thermal cycling test. The major weakness of yttrium and lutetium silicate EBC is the presence of a thermally grown oxide layer at the EBC/SiC interface. This TGO layer is made of cristobalite which exhibits a displacive  $\beta$ -to- $\alpha$  transformation at 200 °C during cooling, accompanied by a volume contraction of about 3-5%. In our coatings, the TGO layer measures less than 10  $\mu\text{m}$  thick which is too thin to induce catastrophic microcracking when samples are thermal cycled.

During water vapor exposition at 1200 °C, the performances of the environmental barrier coatings have been evaluated. Despite the stability of coating materials, the protection was not effective due to the presence of vertical cracks which provide a corrosion path for water vapor to the sensitive SiC substrate and silica TGO layer. Nevertheless, the rare earth silicates have demonstrated their performance as environmental barrier under water vapor by providing an effective corrosion resistance. During the corrosion tests, the coating surface composition has been modified due to the corrosive gases. The presence of Si- and Al-hydroxides in the water vapor jet modifies the chemical equilibrium at EBC surface. This results in an improved stability of rare earth disilicates and the formation of a YAG phase by reaction between Al-hydroxides and yttria or yttrium mono-silicate. In order to improve the custom-oven design, the use of zirconia tubes, replacing the mullite tubes, should provide a water vapor jet without metallic hydroxide impurities.

Therefore, the typical coating structure, related to the SPSS process, seems not suitable for the application of environmental barrier coatings. Efforts have been made to optimize the coating structure by decreasing the coating porosity (Ref 37, 40), but corrosion tests have been unequivocal: environmental barrier coating has to be dense to provide hermeticity.

**Acknowledgments** The authors would like to thank Kossi E. Béré for its technical support during the plasma spray process. They are also grateful to the Center of Characterization of Materials (Sherbrooke, QC, CA) and to NACOMAT partners (Bordeaux, France) for financial support.

## References

1. P. Baldus, M. Jansen, and D. Sporn, Ceramic Fibres for Matrix Composites in High-Temperature Engine Applications, *Science*, 1999, **80**(699), p 699-703. doi:10.1126/science.285.5428.699
2. M. Belmonte, Advanced Ceramic Materials for High Temperature Applications, *Adv. Eng. Mater.*, 2006, **8**, p 693-703. doi:10.1002/adem.200500269
3. A.G. Evans and D.B. Marshall, The Mechanical Behavior of Ceramic Matrix Composites, *Acta Met.*, 1989, **37**, p 2567-2583
4. Y. Katoh, S.M. Dong, and A. Kohyama, Thermo-Mechanical Properties Carbide Composites Fabricated and Microstructure of Silicon by Nano-Infiltrated Transient Eutectoid Process, *Fusion Eng. Des.*, 2002, **61-2**, p 723-731
5. R. Naslain, Design, Preparation and Properties of Non-oxide CMCs for Application in Engines and Nuclear Reactors: An overview, *Compos. Sci. Technol.*, 2004, **64**, p 155-170. doi:10.1016/S0266-3538(03)00230-6
6. R.R. Naslain, Ceramic Matrix Composites: Matrices and Processing, *Encyclopedia Sci. Technol. Mater.*, 2000, doi:10.1016/B978-0-12-803581-8.02317-1
7. A. Misra, 12—Composite Materials for Aerospace Propulsion Related to Air and Space Transportation A2—Njuguna, J BT—Lightweight Composite Structures in Transport, *Light. Compos. Struct. Transp.*, 2016, doi:10.1016/B978-1-78242-325-6.00012-8
8. S.N. Basu and V.K. Sarin, Thermal and Environmental Barrier Coatings for Si-Based Ceramics, *Elsevier*, 2014, doi:10.1016/B978-0-08-096527-7.00036-2
9. N.P. Padture, Advanced Structural Ceramics in Aerospace Propulsion, *Nat. Mater.*, 2016, **15**, p 804-809. doi:10.1038/nmat4687
10. H.E. Eaton and G.D. Linsey, Accelerated Oxidation of SiC CMC's by Water Vapor and Protection via Environmental Barrier Coating Approach, *J. Eur. Ceram. Soc.*, 2002, **22**, p 2741-2747. doi:10.1016/S0955-2219(02)00141-3
11. N. Al Nasiri, N. Patra, N. Ni, D.D. Jayaseelan, and W.E. Lee, Oxidation Behaviour of SiC/SiC Ceramic Matrix Composites in Air, *J. Eur. Ceram. Soc.*, 2016, **36**, p 3293-3302. doi:10.1016/j.jeurceramsoc.2016.05.051
12. N.S. Jacobson, Corrosion of Silicon-Based Ceramics in Combustion Environments, *J. Am. Ceram. Soc.*, 1993, **76**, p 3-28. doi:10.1111/j.1151-2916.1993.tb03684.x
13. E.J. Opila, Oxidation and Volatilization of Silica Formers in Water Vapor, *J. Am. Ceram. Soc.*, 2003, **86**, p 1238-1248. doi:10.1111/j.1151-2916.2003.tb03459.x
14. P.J. Meschter, E.J. Opila, and N.S. Jacobson, Water Vapor-Mediated Volatilization of High-Temperature Materials, *Annu. Rev. Mater. Res.*, 2013, **43**, p 559-588. doi:10.1146/annurev-matsci-071312-121636
15. P.F. Tortorelli and K.L. More, Effects of High Water-Vapor Pressure on Oxidation of Silicon Carbide at 1200 °C, *J. Am. Ceram. Soc.*, 2003, **86**, p 1249-1255. doi:10.1111/j.1151-2916.2003.tb03460.x
16. E.J. Opila and R.E. Hann, Paraline Oxidation of CVD SiC in Water Vapor, *J. Am. Ceram. Soc.*, 1997, **80**, p 197-205. doi:10.1111/j.1151-2916.1997.tb02810.x
17. E. Courcot, F. Rebillat, F. Teyssandier, From the Volatility of Simple Oxides to that of Mixed Oxides: Thermodynamic and Experimental Approaches, in: *Ceram. Trans.*, 2010: pp. 235–244
18. E. Courcot, F. Rebillat, F. Teyssandier, and C. Louchet-Pouillier, Thermochemical Stability of the Y<sub>2</sub>O<sub>3</sub>–SiO<sub>2</sub> System, *J. Eur. Ceram. Soc.*, 2010, **30**, p 905-910. doi:10.1016/j.jeurceramsoc.2009.09.007
19. N. Maier, K.G. Nickel, and G. Rixecker, High Temperature Water Vapour Corrosion of Rare Earth Disilicates (Y, Yb, Lu)<sub>2</sub>Si<sub>2</sub>O<sub>7</sub> in the Presence of Al(OH)<sub>3</sub> Impurities, *J. Eur. Ceram. Soc.*, 2007, **27**, p 2705-2713
20. Y. Wang and J. Liu, First-Principles Investigation on the Corrosion Resistance of Rare Earth Disilicates in Water Vapor, *J. Eur. Ceram. Soc.*, 2009, **29**, p 2163-2167

21. J. Liu, L. Zhang, Q. Liu, L. Cheng, and Y. Wang, Structure Design and Fabrication of Environmental Barrier Coatings for Crack Resistance, *J. Eur. Ceram. Soc.*, 2014, **34**, p 2005-2012. doi:[10.1016/j.jeurceramsoc.2013.12.049](https://doi.org/10.1016/j.jeurceramsoc.2013.12.049)
22. B.T. Richards, K.A. Young, F. De Francqueville, S. Sehr, M.R. Begley, and H.N.G. Wadley, Response of Ytterbium Disilicate-Silicon Environmental Barrier Coatings to Thermal Cycling in Water Vapor, *Acta Mater.*, 2016, **106**, p 1-14. doi:[10.1016/j.actamat.2015.12.053](https://doi.org/10.1016/j.actamat.2015.12.053)
23. F. Stolzenburg, P. Kenesei, J. Almer, K.N. Lee, M.T. Johnson, and K.T. Faber, The Influence of Calcium-Magnesium-Aluminosilicate Deposits on Internal Stresses in  $\text{Yb}_2\text{Si}_2\text{O}_7$  Multilayer Environmental Barrier Coatings, *Acta Mater.*, 2016, **105**, p 189-198. doi:[10.1016/j.actamat.2015.12.016](https://doi.org/10.1016/j.actamat.2015.12.016)
24. K.N. Lee, D.S. Fox, and N.P. Bansal, Rare Earth Silicate Environmental Barrier Coatings for SiC/SiC Composites and  $\text{Si}_3\text{N}_4$  Ceramics, *J. Eur. Ceram. Soc.*, 2005, **25**, p 1705-1715. doi:[10.1016/j.jeurceramsoc.2004.12.013](https://doi.org/10.1016/j.jeurceramsoc.2004.12.013)
25. Z. Tian, L. Zheng, J.J. Wang, P. Wan, J. Li, and J.J. Wang, Theoretical and Experimental Determination of the Major Thermo-Mechanical Properties of  $\text{RE}_2\text{SiO}_5$  (RE = Tb, Dy, Ho, Er, Tm, Yb, Lu, and Y) for Environmental and Thermal Barrier Coating Applications, *J. Eur. Ceram. Soc.*, 2016, **36**, p 189-202. doi:[10.1016/j.jeurceramsoc.2015.09.013](https://doi.org/10.1016/j.jeurceramsoc.2015.09.013)
26. S. Ueno, D. Doni Jayaseelan, H. Kita, T. Ohji, and H.-T. Lin, Comparison of Water Vapor Corrosion Behaviors of  $\text{Ln}_2\text{Si}_2\text{O}_7$  (Ln = Yb and Lu) and  $\text{ASiO}_4$  (A = Ti, Zr and Hf) EBC's, *Key Eng. Mater.*, 2006, **317–318**, p 557-560
27. S. Ueno, D.D. Jayaseelan, and T. Ohji, Water Vapor Corrosion Behavior of Lutetium Silicates at High Temperature, *Ceram. Int.*, 2006, **32**, p 451-455. doi:[10.1016/j.ceramint.2005.03.022](https://doi.org/10.1016/j.ceramint.2005.03.022)
28. S. Ueno, D.D. Jayaseelan, T. Ohji, and H.T. Lin, Recession Mechanism of  $\text{Lu}_2\text{Si}_2\text{O}_7$  Phase in High Speed Steam Jet Environment at High Temperatures, *Ceram. Int.*, 2006, **32**, p 775-778. doi:[10.1016/j.ceramint.2005.05.014](https://doi.org/10.1016/j.ceramint.2005.05.014)
29. N.S. Jacobson, D.S. Fox, J.L. Smialek, E.J. Opila, C. Dellacorte, and K.N. Lee, Performance of Ceramics in Severe Environments. ASM Handbook, *Corros. Mater.*, 2005, doi:[10.1361/asmhba0003842](https://doi.org/10.1361/asmhba0003842)
30. J. Karthikeyan, C.C. Berndt, J. Tikkanen, S. Reddy, and H. Herman, Plasma spray Synthesis of Nanomaterial Powders and Deposits, *Mater. Sci. Eng., A*, 1997, **238**, p 275-286. doi:[10.1016/S0921-5093\(96\)10568-2](https://doi.org/10.1016/S0921-5093(96)10568-2)
31. Y. Shen, V.A.B. Almeida, and F. Gitzhofer, Preparation of Nanocomposite GDC/LSCF Cathode Material for IT-SOFC by Induction Plasma Spraying, *J. Therm. Spray Technol.*, 2011, **20**, p 145-153. doi:[10.1007/s11666-010-9583-z](https://doi.org/10.1007/s11666-010-9583-z)
32. E.H. Jordan, C. Jiang, and M. Gell, The Solution Precursor Plasma Spray (SPPS) Process: A Review with Energy Considerations, *J. Therm. Spray Technol.*, 2015, **24**, p 1153-1165. doi:[10.1007/s11666-015-0272-9](https://doi.org/10.1007/s11666-015-0272-9)
33. C. Jiang, E.H. Jordan, A.B. Harris, M. Gell, and J. Roth, Double-Layer Gadolinium Zirconate/Yttria-Stabilized Zirconia Thermal Barrier Coatings Deposited by the Solution Precursor Plasma Spray Process, *J. Therm. Spray Technol.*, 2015, **24**, p 895-906. doi:[10.1007/s11666-015-0283-6](https://doi.org/10.1007/s11666-015-0283-6)
34. P. Fauchais, A. Vardelle, Advanced Plasma Spray Applications, in: H. Salimi Jazi (Ed.), *Adv. Plasma Spray Appl.*, InTech, 2012, p 149-188. doi:[10.5772/1921](https://doi.org/10.5772/1921).
35. E.H. Jordan, L. Xie, M. Gell, N.P. Padture, B. Cetegen, A. Ozturk et al., Superior Thermal Barrier Coatings using Solution Precursor Plasma Spray, *J. Therm. Spray Technol.*, 2004, **13**, p 57-65. doi:[10.1361/10599630418121](https://doi.org/10.1361/10599630418121)
36. G. Bertolissi, C. Chazelas, G. Bolelli, L. Lusvardi, M. Vardelle, and A. Vardelle, Engineering the Microstructure of Solution Precursor Plasma-sprayed Coatings, *J. Therm. Spray Technol.*, 2012, **21**, p 1148-1162. doi:[10.1007/s11666-012-9789-3](https://doi.org/10.1007/s11666-012-9789-3)
37. É. Darthout and F. Gitzhofer, Structure Stabilization by Zirconia Pinning Effect of  $\text{Y}_2\text{Si}_2\text{O}_7$  Environmental Barrier Coatings Synthesized by Solution Precursor Plasma Spraying Process, *Surf. Coatings Technol.*, 2017, **309**, p 1081-1088. doi:[10.1016/j.surfcoat.2016.10.015](https://doi.org/10.1016/j.surfcoat.2016.10.015)
38. L. Xie, X. Ma, A. Ozturk, E.H. Jordan, N.P. Padture, B.M. Cetegen et al., Processing Parameter Effects on Solution Precursor Plasma Spray Process Spray Patterns, *Surf. Coatings Technol.*, 2004, **183**, p 51-61. doi:[10.1016/j.surfcoat.2003.09.071](https://doi.org/10.1016/j.surfcoat.2003.09.071)
39. P. Fauchais, V. Rat, J.F. Coudert, R. Etchart-Salas, and G. Montavon, Operating Parameters for Suspension and Solution Plasma-Spray Coatings, *Surf. Coatings Technol.*, 2008, **202**, p 4309-4317. doi:[10.1016/j.surfcoat.2008.04.003](https://doi.org/10.1016/j.surfcoat.2008.04.003)
40. E. Darthout, A. Quet, N. Braidy, and F. Gitzhofer,  $\text{Lu}_2\text{O}_3$ - $\text{SiO}_2$ - $\text{ZrO}_2$  Coatings for Environmental Barrier Application by Solution Precursor Plasma Spraying and Influence of Precursor Chemistry, *J. Therm. Spray Technol.*, 2014, **23**, p 325-332. doi:[10.1007/s11666-013-9987-7](https://doi.org/10.1007/s11666-013-9987-7)
41. É. Darthout, G. Laduye, and F. Gitzhofer, Processing Parameter Effects and Thermal Properties of  $\text{Y}_2\text{Si}_2\text{O}_7$  Nanostructured Environmental Barrier Coatings Synthesized by Solution Precursor Induction Plasma Spraying, *J. Therm. Spray Technol.*, 2016, **25**, p 1264-1279. doi:[10.1007/s11666-016-0450-4](https://doi.org/10.1007/s11666-016-0450-4)
42. X.Q. Cao, R. Vassen, and D. Stoeber, Ceramic Materials for Thermal Barrier Coatings, *J. Eur. Ceram. Soc.*, 2004, **24**, p 1-10. doi:[10.1016/S0955-2219\(03\)00129-8](https://doi.org/10.1016/S0955-2219(03)00129-8)
43. C.M. Weyant, K.T. Faber, J. Almer, and J.V. Guiheen, Residual Stress and Microstructural Evolution in Tantalum Oxide Coatings on Silicon Nitride, *J. Am. Ceram. Soc.*, 2005, **88**, p 2169-2176. doi:[10.1111/j.1551-2916.2005.00396.x](https://doi.org/10.1111/j.1551-2916.2005.00396.x)
44. W.D. Kingery, Factors Affecting Thermal Stress Resistance, *J. Am. Ceram. Soc.*, 1955, **38**, p 3-15. doi:[10.1111/j.1151-2916.1955.tb14545.x](https://doi.org/10.1111/j.1151-2916.1955.tb14545.x)
45. J.C. Han, Thermal Shock Resistance of Ceramic Coatings, *Acta Mater.*, 2007, **55**, p 3573-3581. doi:[10.1016/j.actamat.2007.02.007](https://doi.org/10.1016/j.actamat.2007.02.007)
46. A. Saha, S. Seal, B. Cetegen, E. Jordan, A. Ozturk, and S. Basu, Thermo-Physical Processes in Cerium Nitrate Precursor Droplets Injected into High Temperature Plasma, *Surf. Coatings Technol.*, 2009, **203**, p 2081-2091. doi:[10.1016/j.surfcoat.2008.09.018](https://doi.org/10.1016/j.surfcoat.2008.09.018)
47. I. Castillo and R.J. Munz, Transient Heat, Mass and Momentum Transfer of an Evaporating Stationary Droplet Containing Dissolved Cerium Nitrate in a RF Thermal Argon-oxygen Plasma Under Reduced Pressure, *Int. J. Heat Mass Transf.*, 2007, **50**, p 240-256. doi:[10.1016/j.ijheatmasstransfer.2006.06.023](https://doi.org/10.1016/j.ijheatmasstransfer.2006.06.023)
48. G.L. Messing, S.-C. Zhang, and G.V. Jayanthi, Ceramic Powder Synthesis, *J. Am. Ceram. Soc.*, 1993, **76**, p 2707-2726. doi:[10.1111/j.1151-2916.1993.tb04007.x](https://doi.org/10.1111/j.1151-2916.1993.tb04007.x)
49. M.I. Boulos, RF Induction Plasma Spraying: State-of-the-art Review, *J. Therm. Spray Technol.*, 1992, **1**, p 33-40. doi:[10.1007/BF02657015](https://doi.org/10.1007/BF02657015)
50. J.D'Errico, Surface Fitting Using Gridfit, MATLAB Cent. File Exch. (2005). <http://fr.mathworks.com/matlabcentral/fileexchange/8998-surface-fitting-using-gridfit>
51. R.C. Robinson and J.L. Smialek, SiC Recession Caused by  $\text{SiO}_2$  Scale Volatility under Combustion Conditions: I, Experimental Results and Empirical Model, *J. Am. Ceram. Soc.*, 1999, **82**, p 1817-1825. doi:[10.1111/j.1151-2916.1999.tb02004.x](https://doi.org/10.1111/j.1151-2916.1999.tb02004.x)
52. J.L. Smialek, R.C. Robinson, E.J. Opila, D.S. Fox, and N.S. Jacobson, SiC and  $\text{Si}_3\text{N}_4$  Recession Due to  $\text{SiO}_2$  Scale Volatility Under Combustor Conditions, *Adv. Compos. Mater.*, 1999, **8**, p 33-45. doi:[10.1163/156855199X000056](https://doi.org/10.1163/156855199X000056)
53. E.J. Opila, D.S. Fox, and N.S. Jacobson, Mass Spectrometric Identification of Si-O-H(g) Species from the Reaction of Silica

- with Water Vapor at Atmospheric Pressure, *J. Am. Ceram. Soc.*, 1997, **12**, p 1009–1012. doi:[10.1111/j.1151-2916.1997.tb02935.x](https://doi.org/10.1111/j.1151-2916.1997.tb02935.x)
54. J. Welty, G.L. Rorrer, and D.G. Foster, *Fundamentals of Momentum, Heat, and Mass Transfer*, Wiley, Hoboken, 2014
  55. R.A. Svehla, Estimated Viscosities and Thermal Conductivities of Gases At High Temperatures, 1962.
  56. J.O. Hirschfelder, R.B. Bird, and E.L. Spotz, The Transport Properties of Gases and Gaseous Mixtures, *Chem. Rev.*, 1949, **44**, p 205–231
  57. V. Angelici Avincola, D. Cupid, and H.J. Seifert, Thermodynamic Modeling of the Silica Volatilization in Steam Related to Silicon Carbide Oxidation, *J. Eur. Ceram. Soc.*, 2015, **35**, p 3809–3818. doi:[10.1016/j.jeurceramsoc.2015.05.036](https://doi.org/10.1016/j.jeurceramsoc.2015.05.036)
  58. N.S. Jacobson, E.J. Opila, D.L. Myers, and E.H. Copland, Thermodynamics of Gas Phase Species in the Si-O-H System, *J. Chem. Thermodyn.*, 2005, **37**, p 1130–1137. doi:[10.1016/j.jct.2005.02.001](https://doi.org/10.1016/j.jct.2005.02.001)
  59. A. Hashimoto, The Effect of H<sub>2</sub>O Gas on Volatilities of Planet-Forming Major Elements: I. Experimental Determination of Thermodynamic Properties of Ca-, Al-, and Si-hydroxide Gas Molecules And its Application to the Solar Nebula, *Geochim. Cosmochim. Acta*, 1992, **56**, p 511–532. doi:[10.1016/0016-7037\(92\)90148-C](https://doi.org/10.1016/0016-7037(92)90148-C)
  60. R.A. Golden and E.J. Opila, A Method for Assessing the Volatility of Oxides in High-temperature High-velocity Water Vapor, *J. Eur. Ceram. Soc.*, 2016, **36**, p 1135–1147. doi:[10.1016/j.jeurceramsoc.2015.11.016](https://doi.org/10.1016/j.jeurceramsoc.2015.11.016)
  61. S.L. Dos Santos, E. Lucato, O.H. Sudre, and D.B. Marshall, A Method for Assessing Reactions of Water Vapor with Materials in High-speed, High-temperature Flow, *J. Am. Ceram. Soc.*, 2011, **94**, p s186–s195. doi:[10.1111/j.1551-2916.2011.04556.x](https://doi.org/10.1111/j.1551-2916.2011.04556.x)
  62. A.G. Evans and J.W. Hutchinson, The Thermomechanical Integrity of Thin Films and Multilayers, *Acta Metall. Mater.*, 1995, **43**, p 2507–2530. doi:[10.1016/0956-7151\(94\)00444-M](https://doi.org/10.1016/0956-7151(94)00444-M)
  63. J. Kováčik, Correlation Between Young's Modulus and Porosity in Porous Materials, *J. Mater. Sci. Lett.*, 1999, **18**, p 1007–1010. doi:[10.1023/A:1006669914946](https://doi.org/10.1023/A:1006669914946)
  64. B. Himmel, T. Gerber, W. Heyer, and W. Blau, X-ray Diffraction Analysis of SiO<sub>2</sub> Structure, *J. Mater. Sci.*, 1987, **22**, p 1374–1378. doi:[10.1007/BF01233136](https://doi.org/10.1007/BF01233136)
  65. R.L. Withers, J.G. Thompson, and T.R. Welberry, The Structure and Microstructure of  $\alpha$ -Cristobalite and Its Relationship to  $\beta$ -Cristobalite, *Phys. Chem. Miner.*, 1989, **16**, p 517–523. doi:[10.1007/BF00202206](https://doi.org/10.1007/BF00202206)
  66. R.C. Breneman, J.W. Halloran, and A. Arbor, Hysteresis Upon Repeated Cycling Through the Beta-Alpha Cristobalite Transformation, *J. Ceram. Sci. Technol.*, 2015, **62**, p 55–61. doi:[10.4416/JCST2014-00048](https://doi.org/10.4416/JCST2014-00048)
  67. K.N. Lee, D.S. Fox, J.I. Eldridge, D. Zhu, R.C. Robinson, N.P. Bansal et al., Upper Temperature Limit of Environmental Barrier Coatings Based on Mullite and BSAS, *J. Am. Ceram. Soc.*, 2003, **86**, p 1299–1306. doi:[10.1111/j.1151-2916.2003.tb03466.x](https://doi.org/10.1111/j.1151-2916.2003.tb03466.x)
  68. C.V. Cojocar, D. Lévesque, C. Moreau, and R.S. Lima, Performance of Thermally Sprayed Si/mullite/BSAS Environmental Barrier Coatings Exposed to Thermal Cycling in Water Vapor Environment, *Surf. Coatings Technol.*, 2013, **216**, p 215–223. doi:[10.1016/j.surfcoat.2012.11.043](https://doi.org/10.1016/j.surfcoat.2012.11.043)
  69. B.T. Richards, M.R. Begley, and H.N.G. Wadley, Mechanisms of Ytterbium Monosilicate/Mullite/Silicon Coating Failure During Thermal Cycling in Water Vapor, *J. Am. Ceram. Soc.*, 2015, **98**, p 4066–4075. doi:[10.1111/jace.13792](https://doi.org/10.1111/jace.13792)
  70. C.S. Tedmon, The Effect of Oxide Volatilization on the Oxidation Kinetics of Cr and Fe-Cr Alloys, *J. Electrochem. Soc.*, 1966, **113**, p 766. doi:[10.1149/1.2424115](https://doi.org/10.1149/1.2424115)
  71. D.L. Poerschke, R.W. Jackson, and C.G. Levi, Silicate Deposit Degradation of Engineered Coatings in Gas Turbines: Progress Toward Models and Materials Solutions, *Annu. Rev. Mater. Res.*, 2016, **46**, p 235–262
  72. S. Ueno, T. Ohji, and H.T. Lin, Recession Behavior of Lu<sub>2</sub>SiO<sub>5</sub> Under a High Speed Steam Jet at High Temperatures, *Ceram. Int.*, 2011, **37**, p 1185–1189. doi:[10.1016/j.ceramint.2010.11.029](https://doi.org/10.1016/j.ceramint.2010.11.029)
  73. S. Ueno, D.D. Jayaseelan, T. Ohji, N. Kondo, and S. Kanzaki, Comparison of Water Vapor Corrosion Mechanisms of Polycrystalline and Eutectic Lu<sub>2</sub>Si<sub>2</sub>O<sub>7</sub>, *J. Ceram. Process. Res.*, 2004, **5**, p 153–156
  74. B.T. Richards and H.N.G. Wadley, Plasma Spray Deposition of Tri-Layer Environmental Barrier Coatings, *J. Eur. Ceram. Soc.*, 2014, **34**, p 3069–3083. doi:[10.1016/j.jeurceramsoc.2014.04.027](https://doi.org/10.1016/j.jeurceramsoc.2014.04.027)
  75. S. Ueno, D.D. Jayaseelan, and T. Ohji, Development of Oxide-Based EBC for Silicon Nitride, *Int. J. Appl. Ceram. Technol.*, 2004, **1**, p 362–373
  76. S. Ueno, T. Ohji, and H.-T. Lin, Corrosion and Recession of Mullite in Water Vapor Environment, *J. Eur. Ceram. Soc.*, 2008, **28**, p 431–435. doi:[10.1016/j.jeurceramsoc.2007.03.006](https://doi.org/10.1016/j.jeurceramsoc.2007.03.006)
  77. M. Fritsch, H. Klemm, M. Herrmann, and B. Schenk, Corrosion of Selected Ceramic Materials in Hot Gas Environment, *J. Eur. Ceram. Soc.*, 2006, **26**, p 3557–3565. doi:[10.1016/j.jeurceramsoc.2006.01.015](https://doi.org/10.1016/j.jeurceramsoc.2006.01.015)
  78. E.J. Opila and D.L. Myers, Alumina Volatility in Water Vapor at Elevated Temperatures, *J. Am. Ceram. Soc.*, 2004, **87**, p 1701–1705. doi:[10.1111/j.1551-2916.2004.01701.x](https://doi.org/10.1111/j.1551-2916.2004.01701.x)
  79. M. Fritsch and H. Klemm, The Water-Vapour hot Gas Corrosion Behavior of Al<sub>2</sub>O<sub>3</sub>-Y<sub>2</sub>O<sub>3</sub> Materials, Y<sub>2</sub>SiO<sub>5</sub> and Y<sub>3</sub>Al<sub>5</sub>O<sub>12</sub>-Coated Alumina in a Combustion Environment. in: A.W. and E.L.-C.D. Zhu, U. Schulz (Eds.), *Adv. Ceram. Coatings Interfaces Ceram. Eng. Sci. Proc.*, John Wiley, John Wiley & Sons, Inc., Hoboken, NJ, USA, 2006, p 148–159. doi:[10.1002/9780470291320.ch14](https://doi.org/10.1002/9780470291320.ch14)
  80. K.N. Lee, Environmental Barrier Coatings for SiCf/SiC, in: *Ceram. Matrix Compos. Mater. Model. Technol.*, John Wiley & Sons, Inc., 2014: pp. 430–451. doi:[10.1002/9781118832998.ch15](https://doi.org/10.1002/9781118832998.ch15)
  81. W. Richerson, *Modern Ceramic Engineering: Properties, Processing, and Use in Design*, 3rd ed., CRC, Boca Raton, 2006
  82. Z. Sun, Y. Zhou, J. Wang, and M. Li, Thermal Properties and Thermal Shock Resistance of  $\gamma$ -Y<sub>2</sub>Si<sub>2</sub>O<sub>7</sub>, *J. Am. Ceram. Soc.*, 2008, **91**, p 2623–2629. doi:[10.1111/j.1551-2916.2008.02470.x](https://doi.org/10.1111/j.1551-2916.2008.02470.x)
  83. Z. Sun, M. Li, and Y. Zhou, Thermal Properties of Single-Phase Y<sub>2</sub>SiO<sub>5</sub>, *J. Eur. Ceram. Soc.*, 2009, **29**, p 551–557. doi:[10.1016/j.jeurceramsoc.2008.07.026](https://doi.org/10.1016/j.jeurceramsoc.2008.07.026)
  84. H. Le Chatelier, *La Silice et les Silicates*, A. Hermann, Paris, 1914